



CERN-EP-2016-095  
10 April 2016  
rev. 28 April 2016

## Multiplicities of charged pions and unidentified charged hadrons from deep-inelastic scattering of muons off an isoscalar target

The COMPASS Collaboration

### Abstract

Multiplicities of charged pions and unidentified hadrons produced in deep-inelastic scattering were measured in bins of the Bjorken scaling variable  $x$ , the relative virtual-photon energy  $y$  and the relative hadron energy  $z$ . Data were obtained by the COMPASS Collaboration using a 160 GeV muon beam and an isoscalar target ( ${}^6\text{LiD}$ ). They cover the kinematic domain in the photon virtuality  $Q^2 > 1 (\text{GeV}/c)^2$ ,  $0.004 < x < 0.4$ ,  $0.2 < z < 0.85$  and  $0.1 < y < 0.7$ . In addition, a leading-order pQCD analysis was performed using the pion multiplicity results to extract quark fragmentation functions.

Keywords: Deep inelastic scattering, pion multiplicities, fragmentation functions

*(to be submitted to Phys. Lett. B)*

## The COMPASS Collaboration

C. Adolph<sup>9</sup>, J. Agarwala<sup>7</sup>, M. Aghasyan<sup>26</sup>, R. Akhunzyanov<sup>8</sup>, M.G. Alexeev<sup>28</sup>, G.D. Alexeev<sup>8</sup>, A. Amoroso<sup>28,29</sup>, V. Andrieux<sup>22</sup>, N.V. Anfimov<sup>8</sup>, V. Anosov<sup>8</sup>, W. Augustyniak<sup>31</sup>, A. Austregesilo<sup>17</sup>, C.D.R. Azevedo<sup>2</sup>, B. Badełek<sup>32</sup>, F. Balestra<sup>28,29</sup>, J. Barth<sup>5</sup>, R. Beck<sup>4</sup>, Y. Bedfer<sup>22,11</sup>, J. Bernhard<sup>14,11</sup>, K. Bicker<sup>17,11</sup>, E. R. Bielert<sup>11</sup>, R. Birsa<sup>26</sup>, J. Bisplinghoff<sup>4</sup>, M. Bodlak<sup>19</sup>, M. Boer<sup>22</sup>, P. Bordalo<sup>13,a</sup>, F. Bradamante<sup>25,26</sup>, C. Braun<sup>9</sup>, A. Bressan<sup>25,26</sup>, M. Büchele<sup>10</sup>, L. Capozza<sup>22</sup>, W.-C. Chang<sup>23</sup>, C. Chatterjee<sup>7</sup>, M. Chiosso<sup>28,29</sup>, I. Choi<sup>30</sup>, S.-U. Chung<sup>17,b</sup>, A. Cicuttin<sup>27,26</sup>, M.L. Crespo<sup>27,26</sup>, Q. Curiel<sup>22</sup>, S. Dalla Torre<sup>26</sup>, S.S. Dasgupta<sup>7</sup>, S. Dasgupta<sup>25,26</sup>, O.Yu. Denisov<sup>29</sup>, L. Dhara<sup>7</sup>, S.V. Donskov<sup>21</sup>, N. Doshita<sup>34</sup>, V. Duic<sup>25</sup>, W. Dünnweber<sup>c</sup>, M. Dziewiecki<sup>33</sup>, A. Efremov<sup>8</sup>, P.D. Eversheim<sup>4</sup>, W. Eyrich<sup>9</sup>, M. Faessler<sup>c</sup>, A. Ferrero<sup>22</sup>, M. Finger<sup>19</sup>, M. Finger jr.<sup>19</sup>, H. Fischer<sup>10</sup>, C. Franco<sup>13</sup>, N. du Fresne von Hohenesche<sup>14</sup>, J.M. Friedrich<sup>17</sup>, V. Frolov<sup>8,11</sup>, E. Fuchey<sup>22</sup>, F. Gautheron<sup>3</sup>, O.P. Gavrichtchouk<sup>8</sup>, S. Gerassimov<sup>16,17</sup>, F. Giordano<sup>30</sup>, I. Gnesi<sup>28,29</sup>, M. Gorzelli<sup>10</sup>, S. Grabmüller<sup>17</sup>, A. Grasso<sup>28,29</sup>, M. Grosse Perdekamp<sup>30</sup>, B. Grube<sup>17</sup>, T. Grussenmeyer<sup>10</sup>, A. Guskov<sup>8</sup>, F. Haas<sup>17</sup>, D. Hahne<sup>5</sup>, D. von Harrach<sup>14</sup>, R. Hashimoto<sup>34</sup>, F.H. Heinsius<sup>10</sup>, R. Heitz<sup>30</sup>, F. Herrmann<sup>10</sup>, F. Hinterberger<sup>4</sup>, N. Horikawa<sup>18,d</sup>, N. d'Hose<sup>22</sup>, C.-Y. Hsieh<sup>23</sup>, S. Huber<sup>17</sup>, S. Ishimoto<sup>34,e</sup>, A. Ivanov<sup>28,29</sup>, Yu. Ivanshin<sup>8</sup>, T. Iwata<sup>34</sup>, R. Jahn<sup>4</sup>, V. Jary<sup>20</sup>, R. Joosten<sup>4</sup>, P. Jörg<sup>10</sup>, E. Kabuß<sup>14</sup>, B. Ketzer<sup>4</sup>, G.V. Khaustov<sup>21</sup>, Yu.A. Khokhlov<sup>21,f,g</sup>, Yu. Kisselev<sup>8</sup>, F. Klein<sup>5</sup>, K. Klimaszewski<sup>31</sup>, J.H. Koivuniemi<sup>3</sup>, V.N. Kolosov<sup>21</sup>, K. Kondo<sup>34</sup>, K. Königsmann<sup>10</sup>, I. Konorov<sup>16,17</sup>, V.F. Konstantinov<sup>21</sup>, A.M. Kotzinian<sup>28,29</sup>, O.M. Kouznetsov<sup>8</sup>, R. Kuhn<sup>17</sup>, M. Krämer<sup>17</sup>, P. Kremser<sup>10</sup>, F. Krinner<sup>17</sup>, Z.V. Kroumchtein<sup>8</sup>, Y. Kulinich<sup>30</sup>, F. Kunne<sup>22</sup>, K. Kurek<sup>31</sup>, R.P. Kurjata<sup>33</sup>, A.A. Lednev<sup>21</sup>, A. Lehmann<sup>9</sup>, M. Levillain<sup>22</sup>, S. Levorato<sup>26</sup>, J. Lichtenstadt<sup>24</sup>, R. Longo<sup>28,29</sup>, A. Maggiora<sup>29</sup>, A. Magnon<sup>22</sup>, N. Makins<sup>30</sup>, N. Makke<sup>25,26</sup>, G.K. Mallot<sup>11</sup>, C. Marchand<sup>22</sup>, B. Marianski<sup>31</sup>, A. Martin<sup>25,26</sup>, J. Marzec<sup>33</sup>, J. Matoušek<sup>19,26</sup>, H. Matsuda<sup>34</sup>, T. Matsuda<sup>15</sup>, G.V. Meshcheryakov<sup>8</sup>, W. Meyer<sup>3</sup>, T. Michigami<sup>34</sup>, Yu.V. Mikhailov<sup>21</sup>, M. Mikhayenko<sup>4</sup>, E. Mitrofanov<sup>8</sup>, N. Mitrofanov<sup>8</sup>, Y. Miyachi<sup>34</sup>, P. Montuenga<sup>30</sup>, A. Nagaytsev<sup>8</sup>, F. Nerling<sup>14</sup>, D. Neyret<sup>22</sup>, V.I. Nikolaenko<sup>21</sup>, J. Nový<sup>20,11</sup>, W.-D. Nowak<sup>10</sup>, G. Nukazuka<sup>34</sup>, A.S. Nunes<sup>13</sup>, A.G. Olshevsky<sup>8</sup>, I. Orlov<sup>8</sup>, M. Ostrick<sup>14</sup>, D. Panzieri<sup>1,29</sup>, B. Parsamyan<sup>28,29</sup>, S. Paul<sup>17</sup>, J.-C. Peng<sup>30</sup>, F. Pereira<sup>2</sup>, M. Pešek<sup>19</sup>, D.V. Peshekhonov<sup>8</sup>, S. Platchkov<sup>22</sup>, J. Pochodzalla<sup>14</sup>, V.A. Polyakov<sup>21</sup>, J. Pretz<sup>5,h</sup>, M. Quaresma<sup>13</sup>, C. Quintans<sup>13</sup>, S. Ramos<sup>13,a</sup>, C. Regali<sup>10</sup>, G. Reicherz<sup>3</sup>, C. Riedl<sup>30</sup>, M. Roskot<sup>19</sup>, D.I. Ryabchikov<sup>21,g</sup>, A. Rybnikov<sup>8</sup>, A. Rychter<sup>33</sup>, R. Salac<sup>20</sup>, V.D. Samoylenko<sup>21</sup>, A. Sandacz<sup>31</sup>, C. Santos<sup>26</sup>, S. Sarkar<sup>7</sup>, I.A. Savin<sup>8</sup>, T. Sawada<sup>23</sup>, G. Sbrizzai<sup>25,26</sup>, P. Schiavon<sup>25,26</sup>, K. Schmidt<sup>10,j</sup>, H. Schmieden<sup>5</sup>, K. Schönning<sup>11,i</sup>, S. Schopferer<sup>10</sup>, E. Seder<sup>22</sup>, A. Selyunin<sup>8</sup>, O.Yu. Shevchenko<sup>8,\*</sup>, D. Steffen<sup>11,17</sup>, L. Silva<sup>13</sup>, L. Sinha<sup>7</sup>, S. Sirtl<sup>10</sup>, M. Slunecka<sup>8</sup>, J. Smolik<sup>8</sup>, F. Sozzi<sup>26</sup>, A. Srnka<sup>6</sup>, M. Stolarski<sup>13</sup>, M. Sulc<sup>12</sup>, H. Suzuki<sup>34,d</sup>, A. Szabelski<sup>31</sup>, T. Szameitat<sup>10,j</sup>, P. Sznajder<sup>31</sup>, S. Takekawa<sup>28,29</sup>, M. Tasevsky<sup>8</sup>, S. Tessaro<sup>26</sup>, F. Tessarotto<sup>26</sup>, F. Thibaud<sup>22</sup>, F. Tosello<sup>29</sup>, V. Tskhay<sup>16</sup>, S. Uhl<sup>17</sup>, J. Veloso<sup>2</sup>, M. Virius<sup>20</sup>, J. Vondra<sup>20</sup>, T. Weisrock<sup>14</sup>, M. Wilfert<sup>14</sup>, R. Windmolders<sup>5</sup>, J. ter Wolbeek<sup>10,j</sup>, K. Zaremba<sup>33</sup>, P. Zavada<sup>8</sup>, M. Zavertyaev<sup>16</sup>, E. Zemlyanichkina<sup>8</sup>, M. Ziembicki<sup>33</sup> and A. Zink<sup>9</sup>

<sup>1</sup> University of Eastern Piedmont, 15100 Alessandria, Italy

<sup>2</sup> University of Aveiro, Department of Physics, 3810-193 Aveiro, Portugal

<sup>3</sup> Universität Bochum, Institut für Experimentalphysik, 44780 Bochum, Germany<sup>k1</sup>

<sup>4</sup> Universität Bonn, Helmholtz-Institut für Strahlen- und Kernphysik, 53115 Bonn, Germany<sup>k</sup>

<sup>5</sup> Universität Bonn, Physikalisches Institut, 53115 Bonn, Germany<sup>k</sup>

<sup>6</sup> Institute of Scientific Instruments, AS CR, 61264 Brno, Czech Republic<sup>m</sup>

<sup>7</sup> Matrivani Institute of Experimental Research & Education, Calcutta-700 030, India<sup>n</sup>

<sup>8</sup> Joint Institute for Nuclear Research, 141980 Dubna, Moscow region, Russia<sup>o</sup>

<sup>9</sup> Universität Erlangen–Nürnberg, Physikalisches Institut, 91054 Erlangen, Germany<sup>k</sup>

<sup>10</sup> Universität Freiburg, Physikalisches Institut, 79104 Freiburg, Germany<sup>k1</sup>

<sup>11</sup> CERN, 1211 Geneva 23, Switzerland

- <sup>12</sup> Technical University in Liberec, 46117 Liberec, Czech Republic<sup>m</sup>
- <sup>13</sup> LIP, 1000-149 Lisbon, Portugal<sup>p</sup>
- <sup>14</sup> Universität Mainz, Institut für Kernphysik, 55099 Mainz, Germany<sup>k</sup>
- <sup>15</sup> University of Miyazaki, Miyazaki 889-2192, Japan<sup>q</sup>
- <sup>16</sup> Lebedev Physical Institute, 119991 Moscow, Russia
- <sup>17</sup> Technische Universität München, Physik Department, 85748 Garching, Germany<sup>kc</sup>
- <sup>18</sup> Nagoya University, 464 Nagoya, Japan<sup>q</sup>
- <sup>19</sup> Charles University in Prague, Faculty of Mathematics and Physics, 18000 Prague, Czech Republic<sup>m</sup>
- <sup>20</sup> Czech Technical University in Prague, 16636 Prague, Czech Republic<sup>m</sup>
- <sup>21</sup> State Scientific Center Institute for High Energy Physics of National Research Center ‘Kurchatov Institute’, 142281 Protvino, Russia
- <sup>22</sup> CEA IRFU/SPhN Saclay, 91191 Gif-sur-Yvette, France<sup>l</sup>
- <sup>23</sup> Academia Sinica, Institute of Physics, Taipei 11529, Taiwan
- <sup>24</sup> Tel Aviv University, School of Physics and Astronomy, 69978 Tel Aviv, Israel<sup>f</sup>
- <sup>25</sup> University of Trieste, Department of Physics, 34127 Trieste, Italy
- <sup>26</sup> Trieste Section of INFN, 34127 Trieste, Italy
- <sup>27</sup> Abdus Salam ICTP, 34151 Trieste, Italy
- <sup>28</sup> University of Turin, Department of Physics, 10125 Turin, Italy
- <sup>29</sup> Torino Section of INFN, 10125 Turin, Italy
- <sup>30</sup> University of Illinois at Urbana-Champaign, Department of Physics, Urbana, IL 61801-3080, USA
- <sup>31</sup> National Centre for Nuclear Research, 00-681 Warsaw, Poland<sup>s</sup>
- <sup>32</sup> University of Warsaw, Faculty of Physics, 02-093 Warsaw, Poland<sup>s</sup>
- <sup>33</sup> Warsaw University of Technology, Institute of Radioelectronics, 00-665 Warsaw, Poland<sup>s</sup>
- <sup>34</sup> Yamagata University, Yamagata 992-8510, Japan<sup>q</sup>

\* Deceased

<sup>a</sup> Also at Instituto Superior Técnico, Universidade de Lisboa, Lisbon, Portugal

<sup>b</sup> Also at Department of Physics, Pusan National University, Busan 609-735, Republic of Korea and at Physics Department, Brookhaven National Laboratory, Upton, NY 11973, USA

<sup>c</sup> Supported by the DFG cluster of excellence ‘Origin and Structure of the Universe’ ([www.universe-cluster.de](http://www.universe-cluster.de))

<sup>d</sup> Also at Chubu University, Kasugai, Aichi 487-8501, Japan<sup>q</sup>

<sup>e</sup> Also at KEK, 1-1 Oho, Tsukuba, Ibaraki 305-0801, Japan

<sup>f</sup> Also at Moscow Institute of Physics and Technology, Moscow Region, 141700, Russia

<sup>g</sup> Supported by Presidential grant NSH-999.2014.2

<sup>h</sup> Present address: RWTH Aachen University, III. Physikalisches Institut, 52056 Aachen, Germany

<sup>i</sup> Present address: Uppsala University, Box 516, 75120 Uppsala, Sweden

<sup>j</sup> Supported by the DFG Research Training Group Programme 1102 “Physics at Hadron Accelerators”

<sup>k</sup> Supported by the German Bundesministerium für Bildung und Forschung

<sup>l</sup> Supported by EU FP7 (HadronPhysics3, Grant Agreement number 283286)

<sup>m</sup> Supported by Czech Republic MEYS Grant LG13031

<sup>n</sup> Supported by SAIL (CSR), Govt. of India

<sup>o</sup> Supported by CERN-RFBR Grant 12-02-91500

<sup>p</sup> Supported by the Portuguese FCT - Fundação para a Ciência e Tecnologia, COMPETE and QREN, Grants CERN/FP 109323/2009, 116376/2010, 123600/2011 and CERN/FIS-NUC/0017/2015

<sup>q</sup> Supported by the MEXT and the JSPS under the Grants No.18002006, No.20540299 and No.18540281; Daiko Foundation and Yamada Foundation

<sup>r</sup> Supported by the Israel Academy of Sciences and Humanities

<sup>s</sup> Supported by the Polish NCN Grant 2015/18/M/ST2/00550

## 1 Introduction

Hadron production in semi-inclusive measurements of deep-inelastic lepton–nucleon scattering (SIDIS) is one of the most powerful tools to investigate the structure and formation of hadrons. Within the standard framework of leading-twist perturbative QCD (pQCD), factorisation theorems [1] allow one to write the SIDIS cross section as a convolution of hard scattering cross sections, which are calculable in pQCD, with non-perturbative Parton Distribution Functions (PDFs) and Fragmentation Functions (FFs). The PDFs account for the partonic structure of hadrons in the initial state. The FFs encode the details about the hadronisation mechanism that describes the transition from final-state partons into colour-neutral hadrons. Both types of functions are believed to be universal, i.e. process independent, and can be interpreted in leading-order (LO) as number densities. While PDFs have been studied in detail for several decades and are hence known with good precision, new accurate measurements are necessary to constrain the FFs. In what follows, we will restrict ourselves to transverse-momentum-integrated PDFs and FFs.

The universality of FFs allows their determination from different high-energy processes, which provide complementary information on the hadronisation mechanism and cover complementary kinematic ranges. The study of hadron production in the electron–positron annihilation process is particularly well suited because its cross section has no dependence on parton densities and gives direct access to FFs. Measurements cover a wide range in the characteristic hard scale, from 10 GeV for recent data from BELLE [2] and BABAR [3] to 100 GeV at the Z boson mass at LEP [4] and SLAC [5], at which only the singlet combination of FFs is accessible. In spite of the high precision, these  $e^+e^-$  data cannot be used to disentangle quarks from anti-quarks, as they only access the sum of quark and antiquark FFs and hence do not allow for a full flavour separation. Hadron multiplicity data from SIDIS provide charge and full flavour separation of fragmentation functions. The SIDIS data from fixed target experiments explore characteristic hard scales down to 1 GeV. The large kinematic range spanned by the mentioned reactions allows one to study QCD scaling violations, which also constrains the gluon FF. The latter is indirectly probed by hadron-hadron collisions, e.g. at RHIC [6], via single-inclusive hadron production at high transverse momentum [7].

The present Paper reports on COMPASS measurements of multiplicities of charged pions and unidentified charged hadrons in a kinematic range that is larger than the one covered by HERMES [8] and similar to the one covered by EMC [9].

The process  $lN \rightarrow l'hX$  is described by the negative square of the four-momentum transfer  $Q^2 = -q^2$ , the Bjorken variable  $x = -q^2/(2P \cdot q)$  and the fraction of the virtual-photon energy that is carried by the final-state hadron,  $z = (P \cdot p_h)/(P \cdot q)$ . Here,  $q = k - k'$ ,  $P$  and  $p_h$  denote the four-momenta of the virtual photon, the nucleon  $N$  and the observed hadron  $h$  respectively, with  $k$  ( $k'$ ) the four momentum of the incident (scattered) lepton. Additional variables used are the lepton energy fraction carried by the virtual photon,  $y = (P \cdot q)/(P \cdot k)$ , and the invariant mass of the final hadronic system,  $W = \sqrt{(P + q)^2}$ . In order to study the hadronisation mechanism in SIDIS, the relevant observable is the differential multiplicity for hadrons of a specific type  $h$ , which is defined as the differential cross section for hadron production normalised to the differential inclusive DIS cross section:

$$\frac{dM^h(x, z, Q^2)}{dz} = \frac{d^3\sigma^h(x, z, Q^2)/dx dQ^2 dz}{d^2\sigma^{\text{DIS}}(x, Q^2)/dx dQ^2}. \quad (1)$$

Interpreted in pQCD, the cross sections on the right-hand side are expressed in terms of PDFs and FFs and read at leading-order (LO)

$$\frac{d^2\sigma^{\text{DIS}}}{dx dQ^2} = C(x, Q^2) \sum_q e_q^2 q(x, Q^2), \quad \frac{d^3\sigma^h}{dx dQ^2 dz} = C(x, Q^2) \sum_q e_q^2 q(x, Q^2) D_q^h(z, Q^2). \quad (2)$$

Here,  $q(x, Q^2)$  is the quark PDF for the flavour  $q$ ,  $D_q^h(z, Q^2)$  the quark-to-hadron FF,  $C(x, Q^2) = 2\pi\alpha^2(1 + (1 - y)^2)/Q^4$  and  $\alpha$  the fine structure constant. In LO,  $D_q^h$  denotes the number density of hadrons  $h$  produced in the hadronisation of partons of species  $q$ .

## 2 The COMPASS experiment

In this Section a short description of the experimental set-up is given, while a more detailed description can be found in Ref. 10. The measurement was performed in 2006 with the naturally polarised muon beam of the CERN SPS using positive muons of 160 GeV/ $c$ . The beam momentum had a spread of 5%. The intensity was  $4 \times 10^7 \text{ s}^{-1}$  with spills of 4.8s and a cycle time of 16.8s. The momentum of each incoming muon was measured at the end of the beam line with a precision of 0.3%. Before the target, the trajectory of each incoming muon was measured in a set of silicon and scintillating fibre detectors with a precision of 0.2 mrad. The muons were impinging on a longitudinally polarised solid-state target positioned inside a large aperture solenoid. The target consisted of three cells, which were located along the beam one after the other and filled with  $^6\text{LiD}$  immersed in a liquid  $^3\text{He}/^4\text{He}$  mixture. The admixtures of H,  $^3\text{He}$  and  $^7\text{Li}$  in the isoscalar target lead to an effective excess of neutrons of about 0.2%. The direction of the polarisation in the 60cm long middle cell was opposite to that in the two 30cm long outer cells. In the analysis, the data are averaged over the target polarisation for the determination of multiplicities.

The two-stage COMPASS spectrometer was designed to reconstruct scattered muons and produced hadrons in a wide range of angle and momentum. Particle tracking was performed by a variety of tracking detectors before and after the two spectrometer magnets. The direction of the reconstructed tracks at the interaction point is determined with a precision of 0.2 mrad, and the momentum resolution is 1.2% in the first spectrometer stage and 0.5% in the second. Muons are identified downstream of hadron absorbers. A ring imaging Cherenkov counter (RICH) in the first stage is used for pion, kaon and proton separation [11]. It was filled with a  $\text{C}_4\text{F}_{10}$  radiator leading to thresholds for pion, kaon and proton detection of about 2.9 GeV/ $c$ , 9 GeV/ $c$  and 18 GeV/ $c$  respectively. In the central part, photon detection was performed using multi-anode photomultiplier tubes that yielded high photodetection efficiency and a fast response in the high rate environment. In the outer part, multi-wire proportional chambers with CsI cathodes were used to detect the UV Cerenkov photons. The trigger, based on pairs of hodoscopes, selected scattered muons above a minimum scattering angle.

## 3 Data analysis

The data analysis includes event selection, particle identification (PID), acceptance correction as well as corrections for radiative effects and diffractive vector meson production. Differential multiplicities are determined in 3-dimensional  $(x, y, z)$  bins from the acceptance-corrected hadron yields  $N^h$  normalised by the number of DIS events,  $N^{\text{DIS}}$ :

$$\frac{dM^h(x, y, z)}{dz} = \frac{1}{N^{\text{DIS}}(x, y)} \frac{dN^h(x, y, z)}{dz} \frac{1}{A(x, y, z)}. \quad (3)$$

The acceptance correction factor  $A$  takes into account the limited geometric and kinematic acceptance of the spectrometer and the efficiency of event reconstruction. The choice of the  $z$  and  $x$  variables is natural because multiplicities depend mostly on these variables. Because of the strong correlation between  $x$  and  $Q^2$  in the COMPASS fixed-target kinematics, it appears more appropriate to use  $y$  instead of  $Q^2$  as the third variable.

### 3.1 Event and hadron selection

The present analysis is based on events with inclusive triggers that use only information on the scattered muons. Selected events are required to have a reconstructed interaction vertex associated to an incident and a scattered muon track. This vertex has to lie inside the fiducial target volume. The incident muon energy is constrained to the interval  $[140, 180]$  GeV. Events are accepted if  $Q^2 > 1$  (GeV/c)<sup>2</sup>,  $0.004 < x < 0.4$  and  $W > 5$  GeV/c<sup>2</sup>. These requirements select the deep-inelastic scattering regime and exclude the nucleon resonance region. The relative virtual-photon energy is constrained to the range  $0.1 < y < 0.7$  to exclude kinematic regions where the momentum resolution degrades and radiative effects are most pronounced. The number of inclusive DIS events selected for this analysis is  $13 \times 10^6$ , corresponding to an integrated luminosity of  $0.54 \text{ fb}^{-1}$ .

For a selected DIS event, all reconstructed tracks are considered. Hadron tracks must be detected in tracking detectors placed before and after the magnet in the first stage of the spectrometer. The fraction of the virtual-photon energy transferred to a final-state hadron is constrained to  $0.2 \leq z \leq 0.85$ , whereby for an unidentified charged hadron the pion mass is assumed. The lower limit avoids the contamination from target remnant fragmentation, while the upper one excludes muons wrongly identified as hadrons, and it also excludes the region with large diffractive contributions. Further constraints on momentum and polar angle of the hadrons as well as on  $y$  are discussed below.

The corrections for higher-order QED effects are applied on an event-by-event basis taking into account the target composition. For  $N^{\text{DIS}}(x, y)$  they are computed according to the scheme described in Ref. 12. For  $dN^{\text{h}}(x, y, z)$  the elastic and quasielastic radiative tails are subtracted from the correction. The  $z$ -integrated radiative correction factor for the multiplicities is always below 5%. A possible  $z$  dependence of radiative corrections is neglected.

### 3.2 Hadron identification using the RICH detector

Particle identification (PID) is performed using the RICH detector [13]. The identification procedure relies on a likelihood function, which is based upon the number and distribution of photons that are detected in the RICH detector and associated to a charged particle trajectory. The likelihood values are calculated by comparing the measured photo-electron pattern with the one expected for different mass hypotheses ( $\pi$ , K, p), taking the distribution of background photons into account. The mass is assigned to the detected hadron choosing the hypothesis with the maximum likelihood. In order to improve the separation between the different mass hypotheses and thus the sample purity, constraints are imposed on the ratios of the maximum over the other likelihood values.

The purity of the identified hadron samples depends on the probabilities of correct identification and misidentification. The true hadron yields  $N_{\text{true}}$  are obtained by applying an unfolding algorithm to the measured hadron yields  $N_{\text{meas}}$ :

$$N_{\text{true}}^i = \sum_j (\mathbf{P}^{-1})_{ij} \cdot N_{\text{meas}}^j. \quad (4)$$

The RICH PID matrix  $\mathbf{P}$  contains as diagonal elements the efficiencies and as off-diagonal elements the misidentification probabilities. The elements of this  $3 \times 3$  matrix are constrained by  $\sum_j \mathbf{P}_{ij} \leq 1$ , where  $i, j = \{\pi, K, p\}$ . They are determined from real data using samples of  $\pi$ , K or p originating from the decay of  $\text{K}_S^0$ ,  $\phi$  or  $\Lambda$  into two charged particles. The dependence of the RICH performance on the particle momentum  $p_{\text{h}}$  and polar angle  $\theta$  at the RICH entrance is taken into account by determining the RICH PID matrix in 2-dimensional bins of these variables. The  $p_{\text{h}}$  dependence accounts for effects arising from momentum thresholds for particle identification and from saturation at high momentum. The  $\theta$  dependence accounts for varying occupancy and background level in the RICH photon detectors. The polar angle is selected in the range  $10 \text{ mrad} < \theta < 120 \text{ mrad}$ , where the efficiencies are high and precisely measured. The  $\theta$  dependence of  $\mathbf{P}_{ij}$  is relatively weak, so that two bins are sufficient in the analysis. In

order to achieve good pion–kaon separation and high particle identification probabilities for kaons and pions, momenta between  $12\text{ GeV}/c$  and  $40\text{ GeV}/c$  are used. In this range, the momentum dependence of the probabilities of  $\pi^+$ ,  $K^+$  and  $p$  to be identified as  $\pi^+$  is shown in Fig. 1 for the lower  $\theta$  bin in 10 momentum bins. Pions are identified with 98% efficiency up to  $30\text{ GeV}/c$ , where the efficiency starts to decrease. The probability to misidentify kaons and protons as pions is below 2% and 6%, respectively, over all the selected momentum range. Similar values are obtained for  $\pi^-$ . The number  $N_{\text{true}}^{\pi^\pm}$  of identified pions available for the analysis after all PID cuts is  $3.4 \times 10^6$ . Without likelihood cuts, the number of charged hadrons is  $4.6 \times 10^6$ .

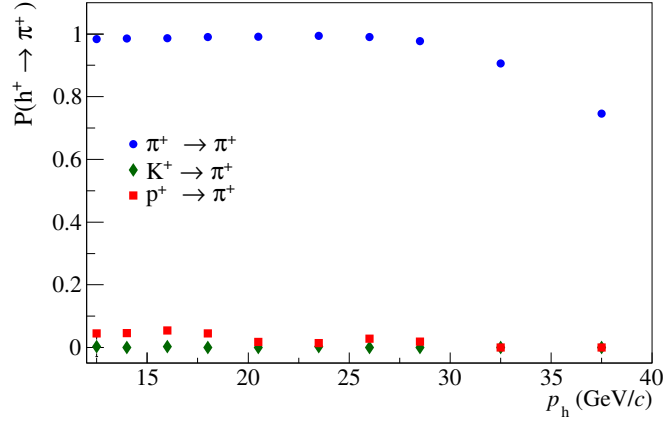


**Figure 1:** Probabilities of RICH identification of  $\pi^+$ ,  $K^+$  and  $p$  as a  $\pi^+$  versus momentum for the smaller  $\theta$  bin  $10\text{ mrad} < \theta < 40\text{ mrad}$ . Statistical uncertainties are lower than the size of the symbols.

### 3.3 Acceptance correction

The raw multiplicities must be corrected for the geometric and kinematic acceptances of the experimental set-up as well as for detector inefficiencies, resolutions and bin migration. The full correction is evaluated using a Monte Carlo (MC) simulation of the muon–nucleon deep-inelastic scattering process. Events are generated with the LEPTO [14] generator, where the parton hadronisation mechanism is simulated using the JETSET package [15] with the tuning from Ref. 16. The spectrometer is simulated using the GEANT3 toolkits [17], and the MC data are reconstructed with the same software as the experimental data [10]. Secondary hadron interactions are simulated using the FLUKA package [18]. The kinematic distributions of the experimental data are fairly well reproduced by the MC simulation.

In order not to introduce a strong dependence on the physics generator used in the simulation, the extraction of hadron multiplicities is performed in narrow kinematic bins of  $x$ ,  $y$  and  $z$ . In each  $(x, y, z)$  bin, the acceptance is calculated from the ratio of reconstructed and generated multiplicities according to

$$A^h(x, y, z) = \frac{dN_{\text{rec}}^h(x, y, z)/N_{\text{rec}}^{\text{DIS}}(x, y)}{dN_{\text{gen}}^h(x, y, z)/N_{\text{gen}}^{\text{DIS}}(x, y)}. \quad (5)$$

The generated kinematic variables are used for the generated particles, while the reconstructed kinematic variables are used for the reconstructed particles. After reconstruction, all particles are subject to the same kinematic and geometric selection criteria as the data, while the generated ones are subject to kinematic requirements only. At this place, the correction for possible misidentification of electrons as pions is included in the acceptance correction. The average value of the acceptance is about 70% for  $y < 0.3$  and about 50% for  $y > 0.3$ . The acceptance is almost flat in  $z$  and  $x$ , except at high  $y$  and low  $x$ , and always larger than 40%.

With the hadron momentum cut, the  $y$  range is more limited for the hadron sample than for the DIS sample. Thus for each bin in  $z$ , the  $y$  range is restricted to the kinematic region accessible with hadron momenta between  $12\text{ GeV}/c$  and  $40\text{ GeV}/c$ .

### 3.4 Vector meson correction

A fraction of the mesons measured in SIDIS originates from diffractive production of vector mesons, which subsequently decay into lighter hadrons. This fraction can be considered as a higher-twist contribution to the SIDIS cross section [8]. It cannot be described by the QCD parton model with the independent-fragmentation mechanism, which is encoded in the FFs. Moreover, fragmentation functions extracted from data including this fraction would be biased, which violates in particular the universality principle of the model. Therefore, the fraction of final-state hadrons originating from diffractive  $\rho^0$  decay is estimated. Our evaluation is based on two MC simulations, one using the LEPTO event generator simulating SIDIS free of diffractive contributions (see Section 3.3), and the other one using the HEPGEN [19] generator simulating diffractive  $\rho^0$  production. Further channels, which are characterised by smaller cross sections, are not taken into account. Events with diffractive dissociation of the target nucleon are also simulated and represent about 25% of those with the nucleon staying intact. The simulation of these events includes nuclear effects, i.e. coherent production and nuclear absorption as described in Ref. 19. A correction factor for the multiplicities is calculated taking into account the diffractive contribution to pion (hadron) and DIS yields. As an example, the  $z$  dependence of the correction factor  $f_{\rho^0}^{\pi}$  for  $\pi^+$  multiplicities is shown in Fig. 2 for three  $Q^2$  bins. The correction varies between 1.02 and 0.55 for pions, with the largest value appearing at small  $Q^2$  and high  $z$ , whereby the latter region is characterised by very small multiplicities.

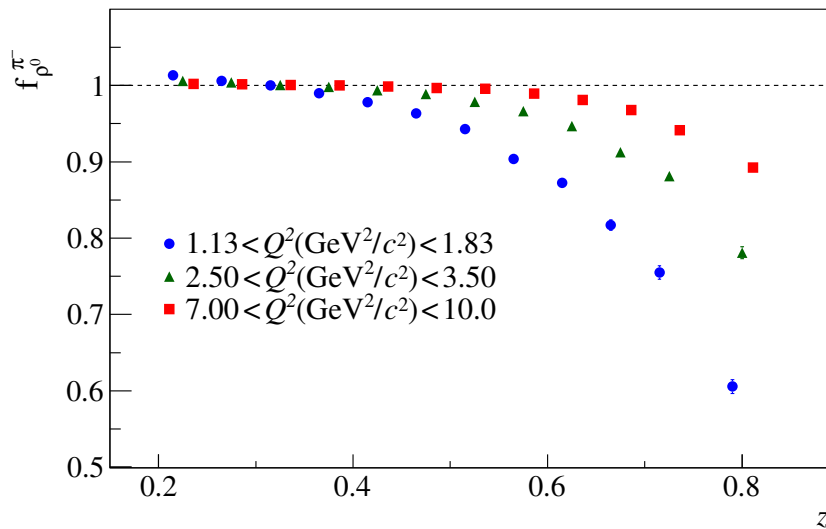


**Figure 2:** Correction due to diffractive  $\rho^0$  contamination, shown for negative-pion multiplicities as a function of  $z$  for three  $Q^2$  bins

### 3.5 Systematic uncertainties

The main contributions to the systematic uncertainties arise from the uncertainties on the determination of the acceptance, of the RICH performance and of the diffractive  $\rho^0$  contribution. The uncertainty on the acceptance calculation is evaluated by two different methods: first, by varying in the MC the PDF set used and the JETSET parameters related to the hadronisation mechanism; secondly, by determining the acceptance in a different dimensional space adding additional variables. The validity of the correction for electron contamination is confirmed by comparing the simulated and measured electron distributions for momenta below  $8 \text{ GeV}/c$ , where electrons are identified using the RICH. An uncertainty of 4% is found that includes the uncertainty of the electron contamination.

In order to estimate the uncertainty linked to the RICH identification and unfolding procedure, different RICH matrices are built by varying the matrix elements within their statistical uncertainties. The dif-



ferences between the resulting multiplicities and the original ones yields an estimate of the uncertainty, which is below 1% for  $z < 0.4$  and reach 2% at high  $z$ . No time dependence is observed when comparing the results obtained from the data taken in six different weeks.

The cross section for exclusive production of  $\rho^0$  calculated in HEPGEN is normalised to the phenomenological model of Ref. 20. The theoretical uncertainty on the predicted cross section close to COMPASS kinematics amounts to about 30%. This results in an uncertainty on the diffractive  $\rho^0$  correction factor, which amounts to at most 30% and depends on the kinematic range.

Nuclear effects may be caused by the presence of  $^3\text{He}/^4\text{He}$  and  $^6\text{Li}$  in the target. A detailed study of such effects was previously performed by the EMC [9] in a similar kinematic range for carbon, copper and tin. A  $z$ -dependent decrease of 5% was observed for the multiplicities of copper compared to the ones of deuterium. While the effect was larger for tin, no such effect was found for carbon, so that possible nuclear effects in the present experiment are expected to be very small and are hence neglected.

All contributions to the systematic uncertainties are added in quadrature and yield the total systematic uncertainty shown as bands in Figs. 5 and 6, which varies between 5% and 10%. Note that not all systematic uncertainties are correlated from bin to bin. It was estimated that, when considering quadratic summation, about 80% of the total systematic uncertainty is correlated from bin to bin. In this case, the remaining 60% is uncorrelated and is treated together with the statistical uncertainties in the fits discussed in Section 5.

#### 4 Results for pion and unidentified hadron multiplicities

The multiplicities presented in the following figures are all corrected for the diffractive  $\rho^0$  contribution. The numerical values are available on HepData [21] for multiplicities with and without this correction. The separate correction factors for DIS and pion (hadron) yields are provided as well. The present results feature a larger data sample, an extended kinematic domain, and an improved treatment of the particle identification, when compared to the results of Ref. 22. The  $x$ ,  $y$  and  $z$  binning used in the analysis is given in Table 1. The  $Q^2$  values range from 1 (GeV/c)<sup>2</sup> at the smallest  $x$  to about 60 (GeV/c)<sup>2</sup> at the highest  $x$ , with  $\langle Q^2 \rangle = 3$  (GeV/c)<sup>2</sup>.

**Table 1:** Bin limits for the three-dimensional binning in  $x$ ,  $y$  and  $z$ .

	bin limits												
$x$	0.004	0.01	0.02	0.03	0.04	0.06	0.1	0.14	0.18	0.4			
$y$	0.1	0.15	0.2	0.3	0.5	0.7							
$z$	0.2	0.25	0.3	0.35	0.4	0.45	0.5	0.55	0.6	0.65	0.7	0.75	0.85

In Figures 3 and 4, the results for the  $z$  and  $y$  dependences of the  $\pi^+$  and  $\pi^-$  multiplicities are presented in the nine bins of  $x$ . Only statistical uncertainties are shown, which are in most cases smaller than the size of the symbols. The curves correspond to the LO pQCD fit as discussed in Section 5.

In Figure 5 multiplicities of positively (closed circles) and negatively (open circles) charged pions are shown versus  $z$ , separately for the nine  $x$  bins but averaged over  $y$ . The error bars correspond to the statistical uncertainties and the bands to the total systematic ones. Figure 6 shows the results for the charged hadron multiplicities. Both figures exhibit a strong dependence on  $z$ , as already observed in previous measurements, and a weak one on  $x$ . Multiplicities are higher for positively than for negatively charged hadrons because of u-quark dominance. This difference is more pronounced for unidentified hadrons than for pions since negative kaons and antiprotons, which are included in the hadron sample, do not contain nucleon valence quarks.

The sum of positively and negatively charged hadron multiplicities integrated over  $z$  is of special interest. As noted in Ref. 23, in the case of kaon multiplicities the sum is used to extract at LO pQCD the

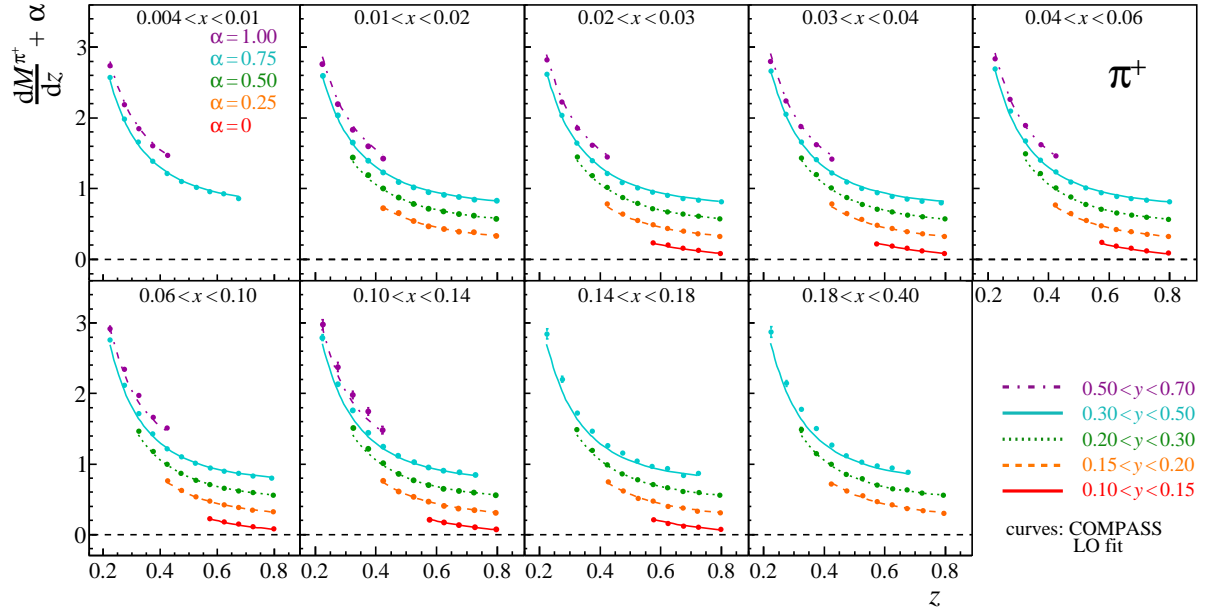


**Figure 3:** Positive pion multiplicities versus  $z$  for nine  $x$  bins and five  $y$  bins (for clarity staggered vertically by  $\alpha$ ). Only statistical uncertainties are shown. The curves correspond to the COMPASS LO fit (see Section 5). (Coloured version online)

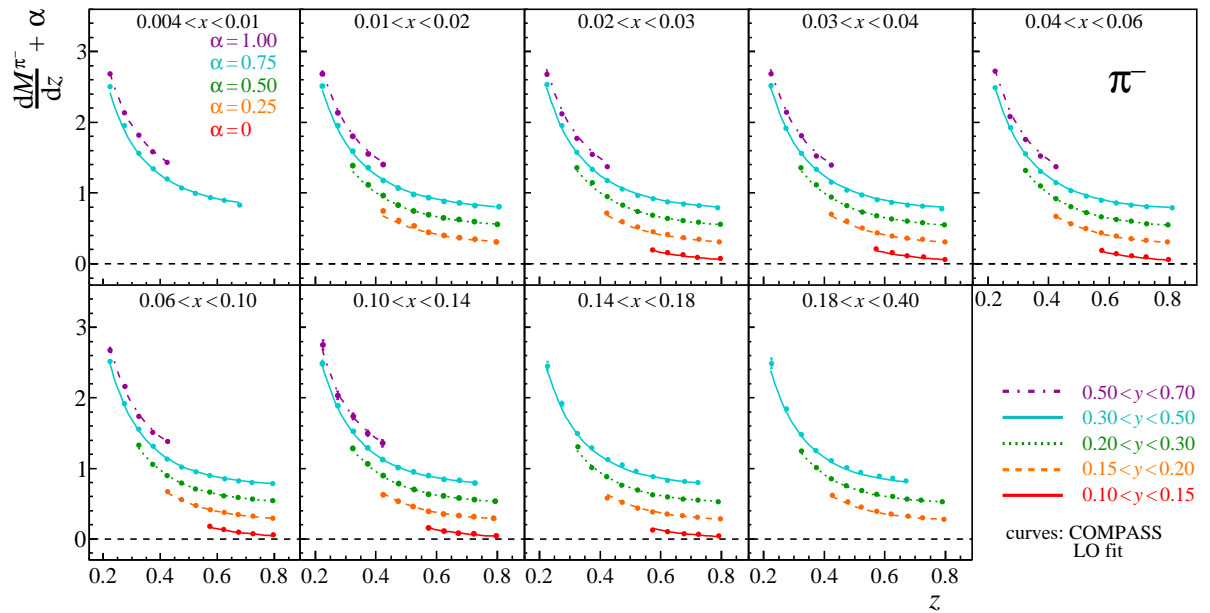


**Figure 4:** Same as Fig. 3 for negative pions. (Coloured version online)

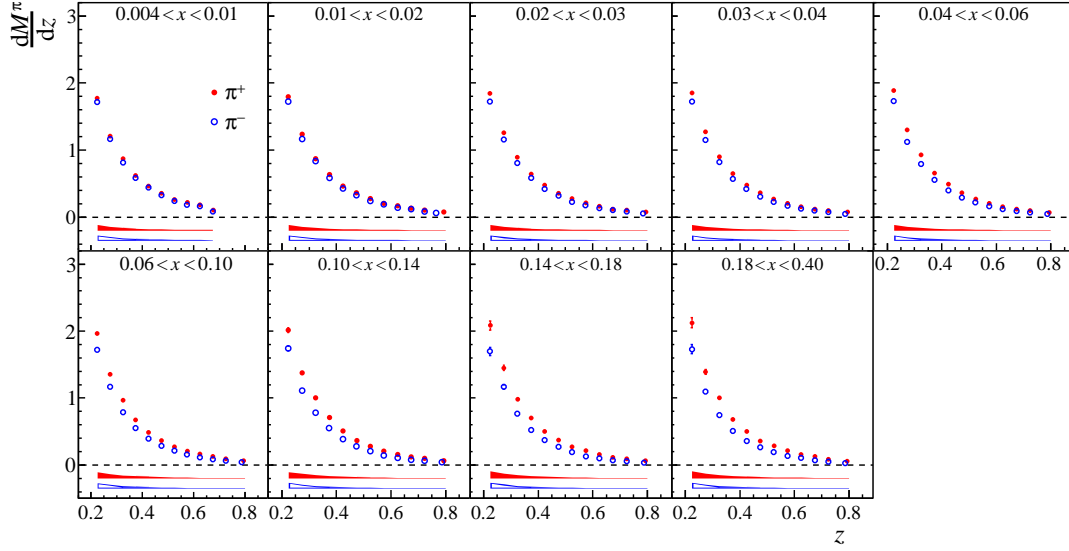


**Figure 5:** Positive (closed) and negative (open) pion multiplicities versus  $z$  for nine  $x$  bins. The bands correspond to the total systematic uncertainties.

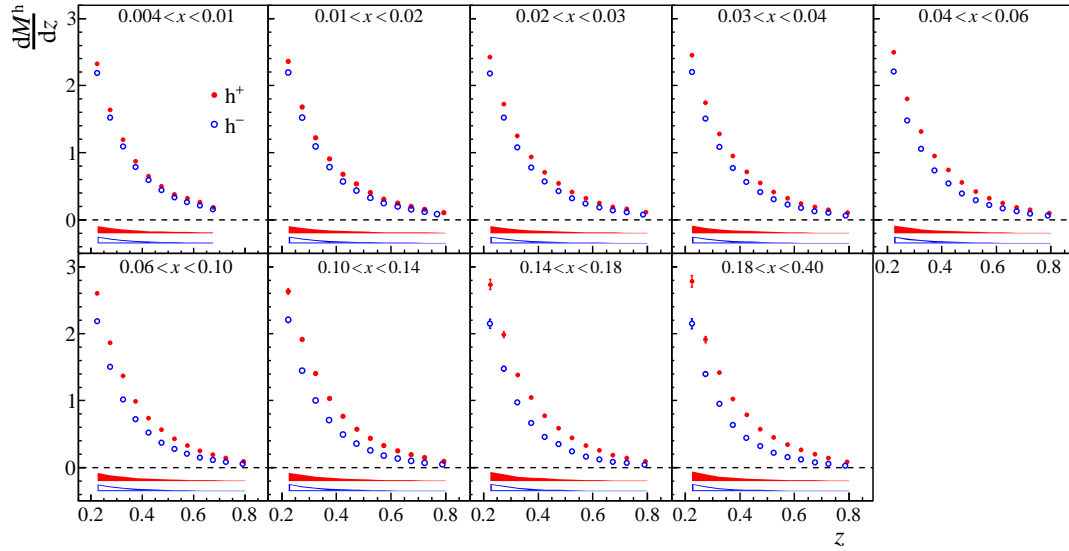


**Figure 6:** Same as Fig. 5 for charged unidentified hadrons.

product of the strange quark distribution and the fragmentation function of strange quarks into kaons. The summed  $\pi^+$  and  $\pi^-$  multiplicities allow us to verify the applicability of the LO pQCD formalism in the COMPASS kinematic domain. For an isoscalar target and taking into account only two independent quark FFs  $D_{\text{fav}}^\pi$  and  $D_{\text{unf}}^\pi$  (see Section 5), the sum of  $\pi^+$  and  $\pi^-$  multiplicities integrated over  $z$  can be written at LO as

$$\mathcal{M}^{\pi^+} + \mathcal{M}^{\pi^-} = \mathcal{D}_{\text{fav}}^\pi + \mathcal{D}_{\text{unf}}^\pi - \frac{2S}{5U + 2S} (\mathcal{D}_{\text{fav}}^\pi - \mathcal{D}_{\text{unf}}^\pi), \quad (6)$$

with  $\mathcal{M}^{\pi^\pm} = \int \langle M^{\pi^\pm}(x, y, z) \rangle_y dz$ . The combinations of PDFs  $U = u + \bar{u} + d + \bar{d}$  and  $S = s + \bar{s}$  depend on  $x$  and  $Q^2$ , and  $\mathcal{D}_{\text{fav}}^\pi(Q^2) = \int D_{\text{fav}}^\pi(z, Q^2) dz$  and  $\mathcal{D}_{\text{unf}}^\pi(Q^2) = \int D_{\text{unf}}^\pi(z, Q^2) dz$  are integrated over the measured  $z$  range and depend on  $Q^2$  only. The pion multiplicity sum is expected to be almost flat in  $x$ , as the term  $2S/(5U + 2S)$  is small and the  $Q^2$  dependence of  $\mathcal{D}_{\text{fav}}^\pi + \mathcal{D}_{\text{unf}}^\pi$  is rather weak (of the order of 3%) [7].

Figure 7 (left) shows the result for the sum  $\mathcal{M}^{\pi^+} + \mathcal{M}^{\pi^-}$  of  $\pi^+$  and  $\pi^-$  multiplicities, integrated over

$z$  from 0.2 to 0.85 and averaged over  $y$  between 0.1 and 0.7, as a function of  $x$ . The expected weak  $x$  dependence is indeed observed in the data. In the same figure, the results of HERMES [8] integrated over  $z$  from 0.2 to 0.8 are shown using the so-called  $x$  representation. The HERMES multiplicities are larger and show a different dependence on  $x$ . Note however that the HERMES data were measured at a lower energy and correspond to different kinematics. In order to compare the COMPASS results also with the EMC ones [9], the sum of unidentified-charged-hadron multiplicities is shown in Fig. 7 (right). The results from COMPASS and EMC, which correspond to comparable kinematics, are found in excellent agreement.

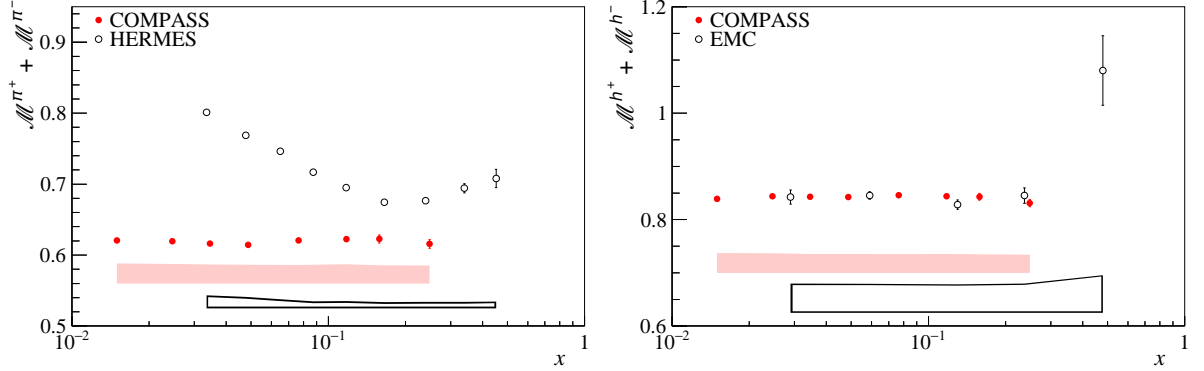


**Figure 7:** Left: Sum of  $\mathcal{M}^{\pi^+}$  and  $\mathcal{M}^{\pi^-}$  versus  $x$ . The COMPASS data (closed circles) are compared to HERMES results (open circles); Right: Sum of  $\mathcal{M}^{h^+}$  and  $\mathcal{M}^{h^-}$  versus  $x$ . The COMPASS data (closed circles) are compared to EMC results (open circles). The systematic uncertainties are shown as bands at the bottom.

Another quantity of interest is the  $x$  dependence of the ratio  $\mathcal{M}^{\pi^+}/\mathcal{M}^{\pi^-}$ , where most experimental systematic effects cancel. The results are shown in Fig. 8 (left) as a function of  $x$ . They are in reasonable agreement with the HERMES values in the measured range. The values obtained from the JLab E00-108 experiment [24] for  $z > 0.3$  at higher  $x$  and lower  $W$  values are also shown for completeness. In Figure 8 (right), the ratio  $\mathcal{M}^{h^+}/\mathcal{M}^{h^-}$  calculated for unidentified hadron multiplicities is shown for COMPASS and EMC data. These results are in excellent agreement.

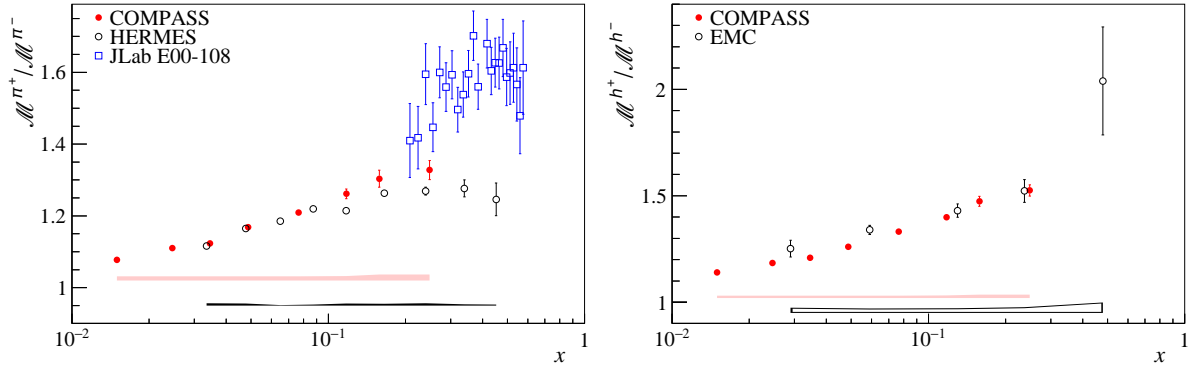


**Figure 8:** Left: Ratio  $\mathcal{M}^{\pi^+}/\mathcal{M}^{\pi^-}$  versus  $x$  from COMPASS (closed points), HERMES (open circles) and JLab E00-108 (open squares). Right: Ratio  $\mathcal{M}^{h^+}/\mathcal{M}^{h^-}$  versus  $x$  for COMPASS (closed circles) and EMC (open circles) results. The systematic uncertainties are shown as bands at the bottom.

## 5 Extraction of quark-to-pion fragmentation functions

The present data on pions cover a wide kinematic range in  $x$  and  $z$  and represent an important input for the extraction of quark-to-pion FFs in future NLO pQCD analyses of the world data. We present here

an extraction of quark-to-pion FFs, however restricted to the present pion data and limited to LO pQCD. The results are checked by performing an independent direct extraction of the two quark FFs in fixed kinematic bins.

The fragmentation of a quark of a given species into a final-state hadron is called favoured if the quark flavour corresponds to a valence quark in the hadron, otherwise the fragmentation is called unfavoured. According to isospin and charge symmetry, and assuming in addition that the strange quark FF is equal to the other unfavoured FFs, only two independent quark-to-pion FFs remain:

$$\begin{aligned} D_{\text{fav}}^{\pi} &= D_{\text{u}}^{\pi^+} = D_{\text{d}}^{\pi^+} = D_{\text{d}}^{\pi^-} = D_{\text{u}}^{\pi^-} \\ D_{\text{unf}}^{\pi} &= D_{\text{d}}^{\pi^+} = D_{\text{u}}^{\pi^+} = D_{\text{u}}^{\pi^-} = D_{\text{d}}^{\pi^-} = D_{\text{s}}^{\pi^{\pm}} = D_{\text{s}}^{\pi^{\pm}}. \end{aligned} \quad (7)$$

A LO pQCD fit to the present set of  $\pi^+$  and  $\pi^-$  multiplicities in  $(x, y, z)$  bins is performed to extract a parametrisation of these two FFs as a function of  $z$ . For the evolution to the  $Q^2$  value of a given data point, the DGLAP  $Q^2$  evolution code of Ref. 25 is used. Even at LO, this evolution involves the additional gluon FF,  $D_{\text{g}}^{\pi} = D_{\text{g}}^{\pi^+} = D_{\text{g}}^{\pi^-}$ . For the PDFs, MSTW08 at LO [26] is used. The following functional form is assumed for the  $z$  dependence of the FFs:

$$zD_i(z) = N_i \frac{z^{\alpha_i}(1-z)^{\beta_i}}{\int_{0.2}^{0.85} z^{\alpha_i}(1-z)^{\beta_i} dz}, \quad (8)$$

where the reference scale is  $Q_0^2 = 1 \text{ (GeV}/c)^2$  and  $i = \{\text{fav}, \text{unf}, \text{g}\}$ . In order to fit simultaneously  $M^{\pi^+}$  and  $M^{\pi^-}$ , a  $\chi^2$  minimisation procedure is applied. It takes into account the quadratic sum of the statistical and uncorrelated systematic uncertainties,  $\Delta^2$ :

$$\chi^2 = \sum_{\pi^+, \pi^-} \sum_{j=1}^N \left[ \left( \frac{\sum_q e_q^2 q(x_j, Q_j^2) D_q^{\pi^{\pm}}(z_j, Q_j^2)}{\sum_q e_q^2 q(x_j, Q_j^2)} - M_{\text{exp}}^{\pi^{\pm}}(x_j, Q_j^2, z_j) \right) / \Delta_j \right]^2, \quad (9)$$

where  $N$  denotes the number of data points. The multiplicities are well described by the fit as shown in Figs. 3 and 4.

The results for the extracted favoured and unfavoured quark FFs and the ratio  $D_{\text{unf}}^{\pi}/D_{\text{fav}}^{\pi}$  are shown in Fig. 9 as a function of  $z$  evolved to  $Q^2 = 3 \text{ (GeV}/c)^2$ . The unfavoured FF is smaller than the favoured one, as expected, and their ratio is seen to decrease with  $z$ . The shaded bands depict the total uncertainty. These bands are determined using a MC sampling method (bootstrap method in Ref. 28). One hundred replicas of the original data set are built by generating standard normal deviates as noise factors that are then multiplied by the data point uncertainties and added to the original data point. For the statistical uncertainty and uncorrelated systematic uncertainty the noise factor is generated for each point separately, while for the correlated systematic uncertainty the noise factor is generated only once per replica. The bands widths are given by the root mean square of the corresponding distributions. Note that for the ratio  $D_{\text{fav}}^{\pi}/D_{\text{unf}}^{\pi}$  most of the correlated systematic uncertainties cancel.

In Figure 9, also recent parametrisations of FFs obtained from NLO analyses by the LSS [29], DSEHS [30] and HKNS [31] groups are compared to the COMPASS LO fit. While the present fit disagrees with the HKNS parametrisation based on electron–positron annihilation data only, qualitative agreement is obtained with the DSEHS and LSS parametrisations that include, in addition to HERMES data, preliminary COMPASS data based on only a fraction of the presently analysed data with a reduced kinematic coverage and larger systematic uncertainties. Therefore, the impact of the present COMPASS results on the global fits will be considerably enhanced when comparing to the impact of the preliminary data discussed in Ref. 22.

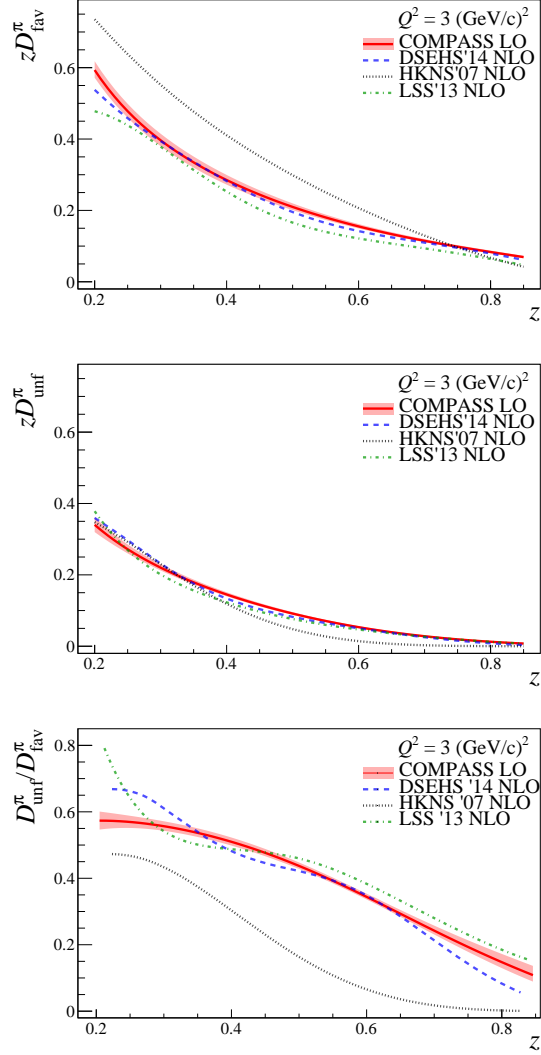


**Figure 9:** Favoured (top) and unfavoured (middle) quark-to-pion FFs and the ratio  $D_{\text{unf}}^{\pi}/D_{\text{fav}}^{\pi}$  (bottom), as obtained from the COMPASS LO fit, compared to the DSEHS, HKNS and LSS fits at NLO. The bands represent the total uncertainties for the FFs and the total statistical uncertainty for the ratio (see text). (Coloured version online)

An alternative method to extract the FFs from the pion multiplicity data is to solve the system of two linear equations for  $M^{\pi^+}$  and  $M^{\pi^-}$  in each  $(x, y, z)$  bin for the values of  $D_{\text{fav}}^{\pi}(\langle z \rangle, \langle Q^2 \rangle)$  and  $D_{\text{unf}}^{\pi}(\langle z \rangle, \langle Q^2 \rangle)$  by using Eqs. (1) and (2). No functional form has to be assumed, and the DGLAP evolution for FFs is not needed. The same PDFs as mentioned above are used. The results from this direct extraction of FFs are in good agreement with the results obtained from the LO fit. This is illustrated in Fig. 10 for one  $(x, y)$  bin.

## 6 Summary and conclusions

We have presented differential multiplicities of charge-separated pions and unidentified charged hadrons measured in SIDIS of muons off an isoscalar target. The results are given in 3-dimensional bins of  $x$ ,  $y$  and  $z$  and cover the kinematic range  $Q^2 > 1 (\text{GeV}/c)^2$ ,  $0.004 < x < 0.4$  and  $0.2 < z < 0.85$ . The numerical values are available in Ref. 21 with and without the subtraction of the contribution of diffractive vector meson production to SIDIS. In addition the radiative corrections factors are provided. These high precision multi-dimensional data provide an important input for future NLO QCD fits of fragmentation functions.

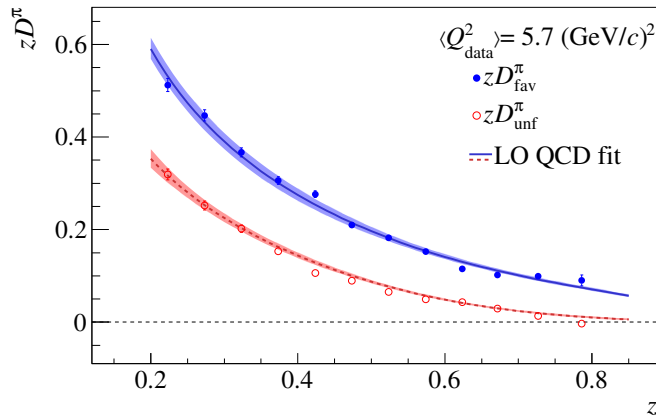


**Figure 10:** The  $z$  dependence of the favoured (closed symbols) and unfavoured (open symbols) quark-to-pion fragmentation functions,  $zD_{\text{fav}}^{\pi}$  and  $zD_{\text{unf}}^{\pi}$ , extracted directly from pion multiplicities for the bin  $0.04 < x < 0.06$  and the bin  $0.1 < y < 0.15$ . For comparison, the result from the present LO QCD fit to the pion multiplicities is shown at  $Q^2 = 6 \text{ (GeV}/c)^2$ . The bands represent the total uncertainties of the QCD fit (see text).

The sum of the  $z$ -integrated positive and negative unidentified hadron and pion multiplicities shows a flat  $x$  behavior, as expected in LO pQCD. For unidentified hadrons this sum is in agreement with EMC results taken at comparable kinematics, whereas some inconsistency is observed when comparing to HERMES pion data that were taken at different kinematics. The ratio of the  $z$ -integrated positive and negative hadron and pion multiplicities as a function of  $x$  nicely confirms the previous measurements from HERMES and EMC.

The measured charged pion multiplicities were used for a LO extraction of the favoured and unfavoured pion FFs. While both FFs are significantly different from those obtained in the HKNS fit to only the electron–positron annihilation data, they are in good agreement with those obtained in recent NLO fits that also include a preliminary release of the present data.

## Acknowledgements

We gratefully acknowledge the support of the CERN management and staff and the skill and effort of the technicians of our collaborating institutes. This work was made possible by the financial support of our funding agencies. Special thanks go to M. Hirai and S. Kumano for providing us with the DGLAP evolution code for fragmentation functions.

## References

- [1] J.C. Collins, D.E. Soper and G.F. Sterman, Nucl. Phys. B 261 (1985) 104.
- [2] BELLE Collaboration, M. Leitgab, et al., Phys. Rev. Lett. 111 (2013) 062002.
- [3] Babar Collaboration, J.P. Lees, et al., Phys. Rev. D 88 (2013) 032011.
- [4] ALEPH Collaboration, R. Barate, et al., Phys. Rep. 294 (1998) 1;  
DEHPI Collaboration, O. Abreu, et al., Eur. Phys. J. C 5 (1998) 585;  
OPAL Collaboration, R. Akers, et al., Z. Phys. C 63 (1994) 181.
- [5] SLD Collaboration, K. Abe, et al., Phys. Rev. D 69 (2004) 072003.
- [6] PHENIX Collaboration, S.S. Adler, et al., Phys. Rev. Lett. 91 (2003) 241803;  
STAR Collaboration, J. Adams, et al., Phys. Rev. Lett. 97 (2006) 152302;  
BRAHMS Collaboration, I. Arsene, et al., Phys. Rev. Lett. 98 (2007) 252001;  
STAR Collaboration, B.I. Abelev, et al., nucl-ex/0607033;

- [7] D. de Florian, R. Sassot and M. Stratmann, *Phys. Rev. D* 75 (2007) 114010.
- [8] HERMES Collaboration, A. Airapetian, et al., *Phys. Rev. D* 87 (2013) 074029.
- [9] EMC, J. Ashman, et al., *Z. Phys. C* 52 (1991) 361.
- [10] COMPASS Collaboration, P. Abbon, et al., *Nucl. Instrum. Meth. A* 577 (2007) 455.
- [11] P. Abbon, et al., *Nucl. Instrum. Meth. A* 616 (2010) 21.
- [12] A.A. Akhundov, D. Bardin, L. Kalinovskaya and T. Riemann, *Fortschr. Phys.* 44 (1996) 373.
- [13] P. Abbon, et al., *Nucl. Instrum. Meth. A* 631 (2011) 26.
- [14] G. Ingelman, A. Edin and J. Rathsman, *Comput. Phys. Commun.* 101 (1997) 108.
- [15] T. Sjostrand, LU-TP-95-20, CERN-TH-7112-93-REV, hep-ph/9508391.
- [16] COMPASS Collaboration, C. Adolph, et al., *Phys. Lett. B* 718 (2013) 922.
- [17] R. Brun, M. Caillat, M. Maire, G. N. Patrick and L. Urban, CERN-DD/85/1.
- [18] T.T. Bohlen, et al., *Nuclear Data Sheets* 120 (2014) 211; A. Ferrari, P.R. Sala, A. Fasso and J. Ranft, CERN-2005-10 (2005), INFN/TC-05/11, SLAC-R-773.
- [19] A. Sandacz and P. Sznajder, HEPGEN - generator for hard exclusive lepton production, arXiv:1207.0333.
- [20] S.V. Goloskokov and P. Kroll, *Eur. Phys. J. C* 53 (2008) 367.
- [21] The Durham HepData Project, <http://durpdg.dur.ac.uk/>.
- [22] N. Makke, Fragmentation function measurement at COMPASS, Proceedings of the 21st Int. Workshop on Deep-Inelastic Scattering and Related Subjects (DIS2013), Marseille, France (2013), PoS DIS2013 (2013) 202.
- [23] HERMES Collaboration, A. Airapetian, et al., *Phys. Lett. B* 666 (2008) 446.
- [24] JLab E00-108, R. Asaturyan, et al., *Phys. Rev. C* 85 (2012) 015202.
- [25] M. Hirai and S. Kumano, *Comput. Phys. Commun.* 183 (2012) 1002.
- [26] A.D. Martin, W.J. Stirling, R.S. Thorne and G. Watt, *Eur. Phys. J. C* 63 (2009).
- [27] LHAPDF homepage, <https://lhapdf.hepforge.org/>.
- [28] W.H. Press, S.A. Teukolsky, W.T. Vetterling and B.P. Flannery, *Numerical Recipes in C (2nd Ed.): The Art of Scientific Computing* 1992.
- [29] E. Leader, A.V. Sidorov and D. Stamenov, Importance of Semi-Inclusive DIS Processes in Determining Fragmentation Functions, Proceedings of the 15th Workshop on High Energy Physics (DSPIN-13), Dubna, Russia (2013), arXiv:1312.5200.
- [30] D. de Florian, et al., *Phys. Rev. D* 91 (2015) 014035.
- [31] M. Hirai, S. Kumano, T.-H. Nagai and K. Sudoh, *Phys. Rev. D* 75 (2007) 094009.